

## Article

# Facile Synthesis of BiVO<sub>4</sub>@ZIF–8 Composite with Heterojunction Structure for Photocatalytic Wastewater Treatment

Runjiang Guo <sup>†</sup>, Yurui Xing <sup>†</sup>, Mengqian Liu, Tanglong Bai, Chaodan Pu <sup>\*</sup> and Hongti Zhang <sup>\*ID</sup>

School of Physical Science and Technology, ShanghaiTech University, Shanghai 201210, China; guorj@shanghaitech.edu.cn (R.G.); xingyr@shanghaitech.edu.cn (Y.X.); liumq@shanghaitech.edu.cn (M.L.); baitl@shanghaitech.edu.cn (T.B.)

<sup>\*</sup> Correspondence: puchd@shanghaitech.edu.cn (C.P.); zhanght3@shanghaitech.edu.cn (H.Z.)

<sup>†</sup> These authors contributed equally to this work.

**Abstract:** Water pollution has always been a serious problem across the world; therefore, facile pollutant degradation via light irradiation has been an attractive issue in the field of environmental protection. In this study, a type of Zn-based metal–organic framework (ZIF–8)-wrapped BiVO<sub>4</sub> nanorod (BiVO<sub>4</sub>@ZIF–8) with high efficiency for photocatalytic wastewater treatment was synthesized through a two-step hydrothermal method. The heterojunction structure of BiVO<sub>4</sub>@ZIF–8 was confirmed by morphology characterization. Due to the introduction of mesoporous ZIF–8, the specific surface area reached up to 304.5 m<sup>2</sup>/g, which was hundreds of times larger than that of pure BiVO<sub>4</sub> nanorods. Furthermore, the band gap of BiVO<sub>4</sub>@ZIF–8 was narrowed down to 2.35 eV, which enabled its more efficient utilization of visible light. After irradiation under visible light for about 40 min, about 80% of rhodamine B (RhB) was degraded, which was much faster than using pure BiVO<sub>4</sub> or other BiVO<sub>4</sub>-based photocatalysts. The synergistic photocatalysis mechanism of BiVO<sub>4</sub>@ZIF–8 is also discussed. This study might offer new pathways for effective degradation of wastewater through facile design of novel photocatalysts.

**Keywords:** nanorods; metal–organic framework; heterojunction photocatalyst; wastewater treatment



**Citation:** Guo, R.; Xing, Y.; Liu, M.; Bai, T.; Pu, C.; Zhang, H. Facile Synthesis of BiVO<sub>4</sub>@ZIF–8 Composite with Heterojunction Structure for Photocatalytic Wastewater Treatment. *Materials* **2021**, *14*, 7424. <https://doi.org/10.3390/ma14237424>

Academic Editor: Vlassios Likodimos

Received: 26 October 2021

Accepted: 29 November 2021

Published: 3 December 2021

**Publisher's Note:** MDPI stays neutral with regard to jurisdictional claims in published maps and institutional affiliations.



**Copyright:** © 2021 by the authors. Licensee MDPI, Basel, Switzerland. This article is an open access article distributed under the terms and conditions of the Creative Commons Attribution (CC BY) license (<https://creativecommons.org/licenses/by/4.0/>).

## 1. Introduction

Recently, water purifying technology has received widespread attention as an emerging field. In particular, photocatalytic degradation is recognized as the most promising way to purify wastewater, due to its low cost and environmentally friendly properties [1–4]. Photocatalysts can degrade noxious organic pollutants under the irradiation of sunlight without producing any toxic remains [5,6]. The key to realizing this advantage relies on precise design of the photocatalysts.

Metal oxide semiconductors, such as TiO<sub>2</sub> (P25), ZnO, Bi<sub>2</sub>O<sub>3</sub>, BiFeO<sub>3</sub>, ZnSnO<sub>3</sub> and BiVO<sub>4</sub>, have all been proved to be efficient photocatalysts [7–14]. Among the many currently studied photocatalysts, BiVO<sub>4</sub>, as a cost-effective, eco-friendly and chemically stable material has garnered considerable interest recently. As indicated in previous studies, monoclinic scheelite, tetragonal zircon and tetragonal scheelite are the most common forms of BiVO<sub>4</sub> existing in nature [15,16]. Compared with tetragonal BiVO<sub>4</sub>, which mainly responds to UV light, BiVO<sub>4</sub> with a monoclinic scheelite structure has better photon harvesting and more sensitive light response properties due to its relatively narrower band gap (2.4 eV); therefore, m-BiVO<sub>4</sub> can generate electron–hole pairs under the irradiation of visible light [17,18]. Recently, many efforts have been made to enhance the photocatalytic properties of BiVO<sub>4</sub>. Guo et al. synthesized V<sup>4+</sup> self-doped BiVO<sub>4</sub> nanorods with [010] oriented for water purification. In these nanorods, the oxygen vacancies and V<sup>4+</sup> ions could act as charge carrier traps and adsorption sites, thus inhibiting the recombination of photogenerated electron–hole pairs, and resulting in an excellent photocatalyst [19].

Photocatalysts' size and shape can also influence their degradation efficiency. Currently, mainstream photocatalysts are often in a solid bulk shape. However, bulk-shaped photocatalysts always suffer from an increased electron–hole recombination rate, poor electron transportation mobility and worse surface absorbability [20,21]. Therefore, investigating photocatalysts with mesoporous structures has attracted a significant amount of attention. Compared with solid photocatalysts, photocatalysts with mesoporous structures have a relatively larger specific surface area. With the enlarged specific surface area, there will be more contact between organic dyes and the catalyst, thus improving the absorption and photodegradation process [22,23]. Metal–organic frameworks (MOFs), as a type of superior mesoporous material, could be prominent host candidates for water splitting due to their high surface area, mesoporous structure, tunable shape and chemical stability [24]. There are a large number of organic ligands around central metal ions, and the chemical bonds between the organic ligands and metal ions are also flexible. Therefore, MOFs can absorb photons and transfer electrons to the metal ions easily. In addition, the synthesis processes for MOFs are convenient. MOFs are usually synthesized by mixing the aromatic multicarboxylate ligands and metal ions in organic solutions, which is much more convenient than other synthesis methods. Thus, MOFs can be prominent candidates for photodegradation [25–27].

Photocatalysts with a single component readily suffer from rapid electron–hole recombination. Therefore, incorporating metal oxide semiconductors and MOFs together might form new types of photocatalysts with improved photocatalytic efficiency by combining their advantages. In addition, to take advantage of the extremely large surface area of MOFs, which can provide more active sites for dye degradation, a semiconductor–MOF heterojunction can be formed at the interface; this can generate an in-built electric field and inhibit rapid electron–hole recombination, thus enhancing their life time and improving photocatalytic efficiency [28,29]. Moreover, the heterojunction can change the distribution of photogenerated electron–hole pairs in order to adjust the band gap width and promote photocatalytic performance [30].

In this research, ZIF–8-wrapped BiVO<sub>4</sub> nanorods with a narrower band gap and larger specific surface area were fabricated through hydrothermal and self-sedimentation processes. The photocatalytic performance of BiVO<sub>4</sub>@ZIF–8 was evaluated by the degradation of RhB solutions. With the newly designed composites, about 70% of the organic dye could be degraded under irradiation with visible light for nearly 40 min. The mechanism of this synergistic photocatalysis was also investigated.

## 2. Materials and Methods

### 2.1. Material Synthesis

#### 2.1.1. Material Preparation

Bismuth nitrate pentahydrate (Bi(NO<sub>3</sub>)<sub>3</sub>·5H<sub>2</sub>O), zinc nitrate hexahydrate (Zn(NO<sub>3</sub>)<sub>2</sub>·6H<sub>2</sub>O), sodium oleate (C<sub>17</sub>H<sub>33</sub>CO<sub>2</sub>Na ≥ 98%), ammonium vanadate (NH<sub>4</sub>VO<sub>3</sub> ≥ 98%), ammonium hydroxide and nitric acid were all bought from Sinopharm Chemical Reagent Co., Ltd. 2-Methylimidazole (C<sub>4</sub>H<sub>6</sub>N<sub>2</sub> ≥ 98%) was purchased from Macklin Inc.

#### 2.1.2. Synthesis of BiVO<sub>4</sub> Nanorods

BiVO<sub>4</sub>@ZIF–8 was synthesized via a two-step method. Typically, the BiVO<sub>4</sub> precursor was synthesized via hydrothermal reaction first, and then the final BiVO<sub>4</sub>@ZIF–8 product was obtained via a self-sedimentation method. In detail, about 0.4 mmol (0.388 g) of bismuth nitrate pentahydrate was dispersed into 20 mL of deionized water under constant stirring. In order to obtain a homogeneous transparent solution, several drops of HNO<sub>3</sub> were added to the mixture. We defined this solution as A. Likewise, 0.4 mmol (0.096 g) NH<sub>4</sub>VO<sub>3</sub> and 1 mmol (0.36 g) sodium oleate were dissolved in deionized water, giving solutions which were defined as B and C, respectively. After 30 min magnetic stirring, we mixed solutions A, B and C together to form a yellow homogeneous suspension. Several drops of ammonium hydroxide were then dropped into the suspension to keep it weakly

alkaline (pH  $\approx$  9). Afterwards, the suspension was poured into a PTFE-made hydrothermal reactor (Yu hua Tech Co., Ltd. Shanghai, China), to be kept at 180 °C for 24 h. After the reaction, the brown powder was collected by centrifugation and dried at 80 °C. To enhance its crystallinity, the BiVO<sub>4</sub> powder was further annealed in a furnace at 450 °C for 2 h.

The second step was to obtain ZIF-8-wrapped BiVO<sub>4</sub>, named BiVO<sub>4</sub>@ZIF-8, via a self-sedimentation method. Typically, we dissolved 0.5 g Zn(NO<sub>3</sub>)<sub>2</sub>·6H<sub>2</sub>O and 0.8 g 2-methylimidazole separately into absolute methanol to form homogeneous solutions. Then, 1 g as-prepared BiVO<sub>4</sub> was dispersed into Zn(NO<sub>3</sub>)<sub>2</sub> solution under vigorous stirring for half an hour. Afterwards, we mixed them together to form a yellow homogeneous suspension and let it stand for half a day. After the reaction, the light yellow powder was collected by centrifugation and dried at 80 °C. The final product was a light yellow BiVO<sub>4</sub>@ZIF-8 composite.

## 2.2. Material Characterization

A JSM-IT500HR/LA instrument (JEOL, Tokyo, Japan) was used for scanning electron microscopy (SEM); a JEM-2100Plus (JEOL, Tokyo, Japan) was used as a transmission electron microscope (TEM); and X-ray diffraction (XRD, D2 Advance, BRUKER, Karlsruhe, Germany) and X-ray photoelectron spectroscopy (XPS, ESCALAB 250Xi, Thermo Fisher Scientific, London, UK) were used to investigate the phase and element information of the final products. Belsorp-MAXII (MicrotracBEL, Osaka, Japan) was used to measure the BET surface area. In this study, the photoluminescence spectra were acquired using a photoluminescence spectrometer (Fluorolog-3 Horiba Scientific, NJ, USA), with 360 nm excitation light. Ultraviolet-visible (UV-Vis) spectra were recorded by a Cary 5000 spectrophotometer (Agilent Technologies, Penang, Malaysia).

## 2.3. Photocatalytic Activity Evaluation

Rhodamine B (RhB) was used to assess the photocatalytic activity of the as-prepared catalyst. Typically, we dispersed 100 mg catalyst (pure BiVO<sub>4</sub> or BiVO<sub>4</sub>@ZIF in this work) into RhB solution with a concentration of 0.5 mg/50 mL. Before the degradation reaction, the suspension was kept in a dark environment for 30 min to reach a photoequilibrium state, using ultrasonic vibration. In the catalysis process, we collected the suspension every 10 min via centrifugation. As the characteristic absorption peak for RhB is at 550 nm, the intensity of the absorption peak for RhB was measured by UV-Vis absorption spectra. Equation (1) below was applied to determine the RhB degradation efficiency (the ratio of the remaining RhB concentration and the initial RhB concentration) in the degradation process:

$$\eta_{eff} = \left(1 - \frac{A_t}{A_0}\right) \times 100\% \quad (1)$$

where  $\eta_{eff}$  is the degradation efficiency of RhB, and  $A_0$  and  $A_t$  are the intensities of absorption peaks before and after degradation for a certain time interval, respectively.

## 3. Results and Discussion

The phase and crystal structure information of the as-synthesized BiVO<sub>4</sub> nanorods and BiVO<sub>4</sub>@ZIF-8 composites was examined by XRD analysis, as shown in Figure S1 (which can be found in the Supplementary Materials) and Figure 1, respectively. In Figure S1, all of the diffraction peaks were assigned to the standard monoclinic-type BiVO<sub>4</sub> (JCPDS card no. 14-0688; a = 5.195 Å, b = 11.704 Å, c = 5.092 Å; space group: I2/a) [31]. There was a minor diffraction peak at 15.11° in the XRD pattern of BiVO<sub>4</sub>, which could distinguish m-BiVO<sub>4</sub> from tetragonal scheelite BiVO<sub>4</sub> (t-BiVO<sub>4</sub>) [32]. It can also be seen in Figure S1 that the intensities of the diffraction peaks of m-BiVO<sub>4</sub> were very strong, suggesting that the defect intensity of BiVO<sub>4</sub> nanorods was notably reduced via calcination. The lower number of defects and high crystallinity of BiVO<sub>4</sub> are conducive to its enhanced catalytic performance, since defects in crystal lattices can play the role of combining centers for photogenerated electrons and holes [33–35]. In addition, there were two diffraction peaks

of  $\text{BiVO}_4$  assigned to (200) and (002) at about  $35^\circ$ , which are characteristic of monoclinic scheelite-type  $\text{BiVO}_4$ . The curve in Figure 1 shows the XRD pattern of  $\text{BiVO}_4@ZIF-8$ . The majority of diffraction peaks of ZIF-8 were clearly seen between  $10^\circ$  and  $30^\circ$ , indicating the co-existence of  $\text{BiVO}_4$  and ZIF-8. We conclude that the  $\text{BiVO}_4@ZIF-8$  composites were formed simply by the attachment of ZIF-8 nanoparticles to the surface of  $\text{BiVO}_4$  nanorods, and that no compound was formed.

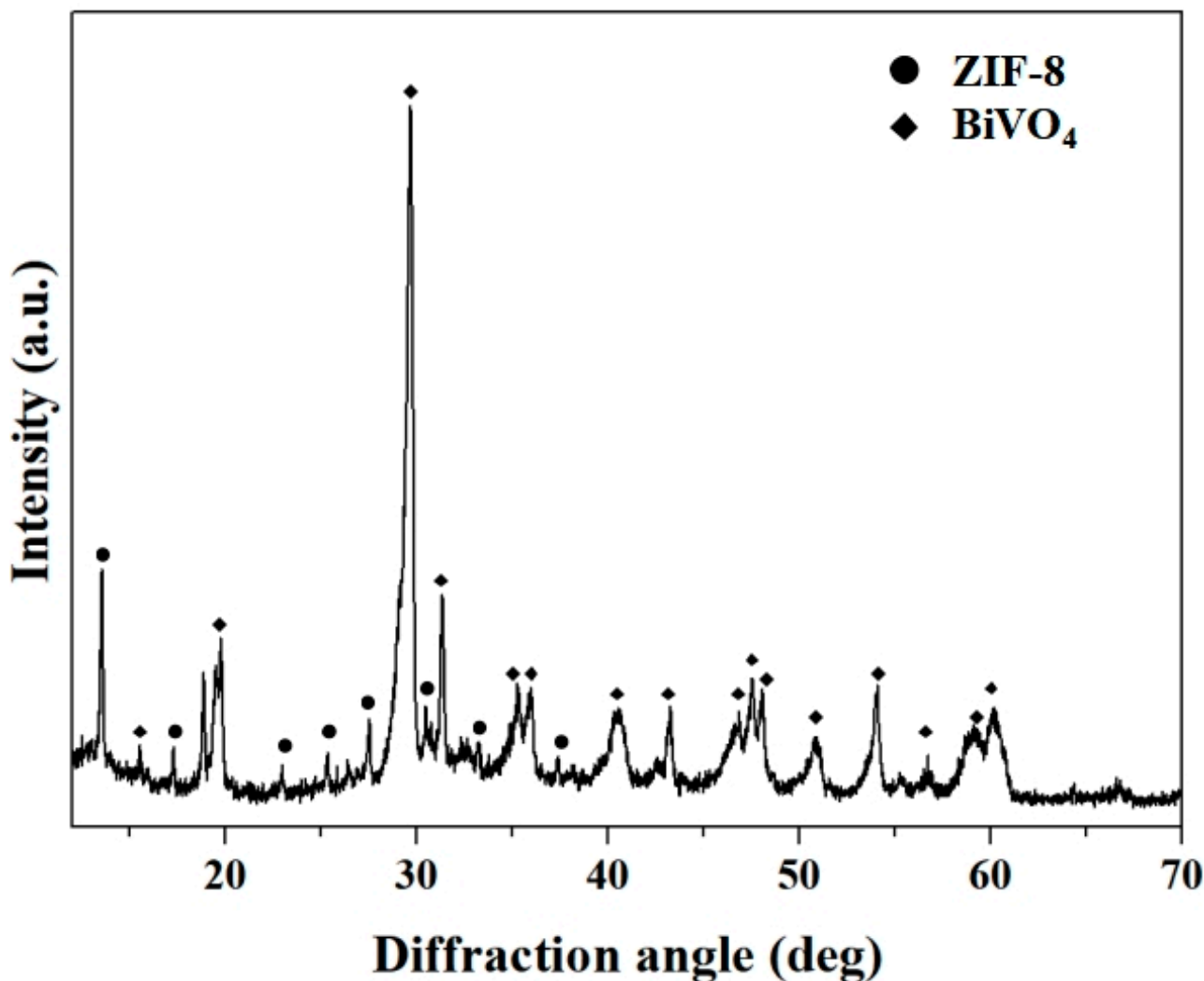


**Figure 1.** The XRD pattern of  $\text{BiVO}_4@ZIF-8$ . The diffraction peaks are assigned to  $\text{BiVO}_4$  and ZIF-8 as indicated.

Morphologies of as-synthesized  $\text{BiVO}_4$  nanorods and  $\text{BiVO}_4@ZIF-8$  composites were obtained by SEM and TEM and are shown in Figure 2a–f. As indicated in Figure 2a–c, the diameter and length of  $\text{BiVO}_4$  nanorods were about 150 nm and 3000 nm, respectively. In addition, the  $\text{BiVO}_4$  nanorods were aggregated together to form a flower-like shape. Figure 2c (insert) shows the HR-TEM image of an individual  $\text{BiVO}_4$  nanorod and its corresponding SAED pattern. As shown in Figure 2c (insert), the diffraction fringes of  $\text{BiVO}_4$  nanorods with the spacing of 0.582 nm were well assigned to their (020) lattice planes ( $b = 11.704\text{\AA}$ , two times the fringe spacing), indicating that the  $\text{BiVO}_4$  nanorods were probably growing along the [010] direction. Figure 2c (insert) also shows the diffraction spots along the [102] zone axis in the SAED pattern. There were two spots around the (000) spots, indexed as the (020) and (211) lattice planes. In addition, there was only one set of diffraction spots in our SAED pattern, indicating that the as-synthesized  $\text{BiVO}_4$  was a pure phase without any impurities. Figure 2d–f show SEM and TEM images of  $\text{BiVO}_4@ZIF-8$ .

The surface of BiVO<sub>4</sub>@ZIF-8 nanorods was coarser than that of pure BiVO<sub>4</sub>. In addition, the BiVO<sub>4</sub>@ZIF-8 nanorods were well dispersed, owing to the existence of the MOF. We could clearly see that ZIF-8 nanoparticles with a size of ~30 nm were tightly attached to the BiVO<sub>4</sub> nanorod's surface and that a heterojunction between the BiVO<sub>4</sub> and ZIF-8 was formed, which could enhance the photocatalysis performance of BiVO<sub>4</sub>@ZIF-8.

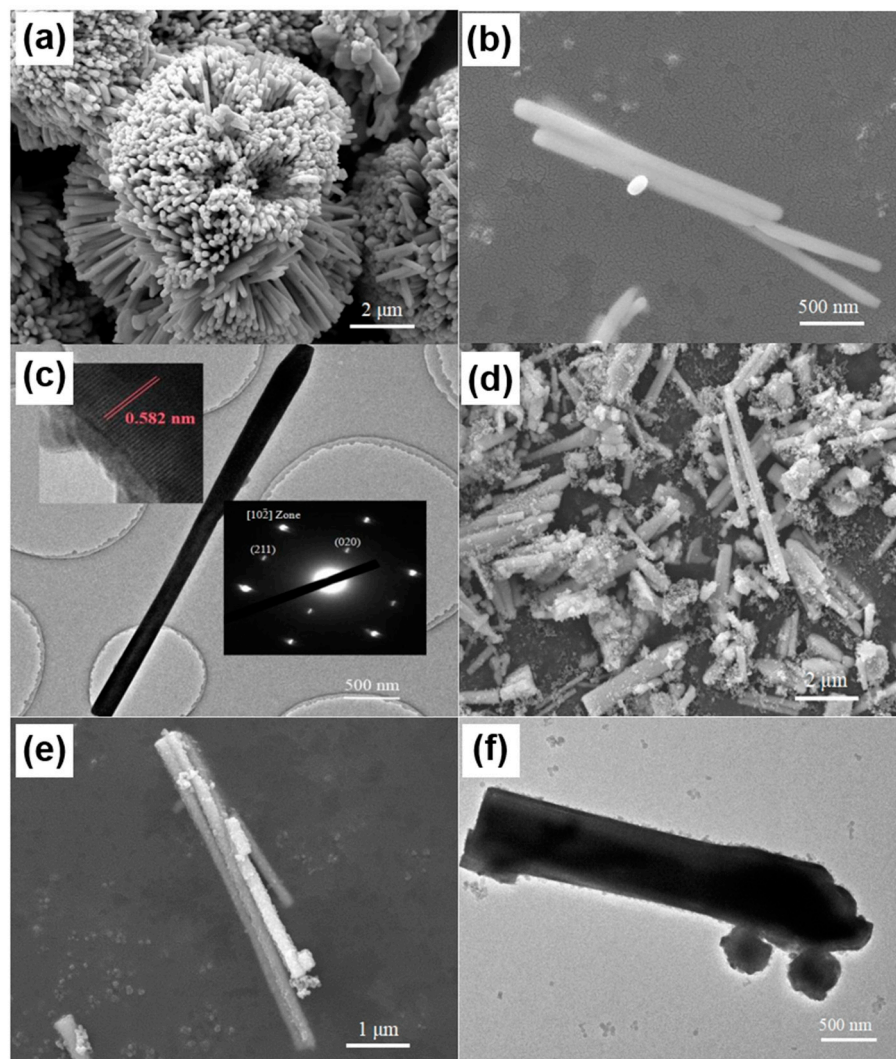


**Figure 2.** Morphology and structure characterization of BiVO<sub>4</sub> and BiVO<sub>4</sub>@ZIF-8. Typical SEM images of as-synthesized BiVO<sub>4</sub> precursor at (a) low and (b) high magnification; typical (c) TEM image with HR-TEM and SAED images inserted of as-synthesized BiVO<sub>4</sub> precursor with the length of ~3000 nm and width of ~150 nm; typical SEM images of as-synthesized BiVO<sub>4</sub>@ZIF-8 at (d) low and (e) high magnification; (f) typical TEM image of as-synthesized BiVO<sub>4</sub>@ZIF-8 with the ZIF-8 nanoparticles tightly attached to the surface of the BiVO<sub>4</sub> nanorod.

XPS (seen in Figure 3a) showed that only Bi, V, C and O existed in as-prepared BiVO<sub>4</sub>. Figure 3b,c show the characteristic peaks for Bi<sup>3+</sup> and V<sup>5+</sup> in BiVO<sub>4</sub>. The binding energies of Bi 4f<sub>7/2</sub> and Bi 4f<sub>5/2</sub> were 158.5 and 164.4 eV, respectively, and the binding energies of V 2p<sub>3/2</sub> and V 2p<sub>1/2</sub> were 516.5 eV and 524.3 eV, respectively, consistent with previous reports [36,37]. The appearance of the C 1s signal at 284.8 eV might be an instrument error during the XPS test. It is noticeable that, in Figure 3d, the O 1s peaks were split into two peaks, which correspond to the O element in the BiVO<sub>4</sub> crystal lattice (528.9 eV) and O<sub>2</sub> absorbed via BiVO<sub>4</sub> (532.5 eV).

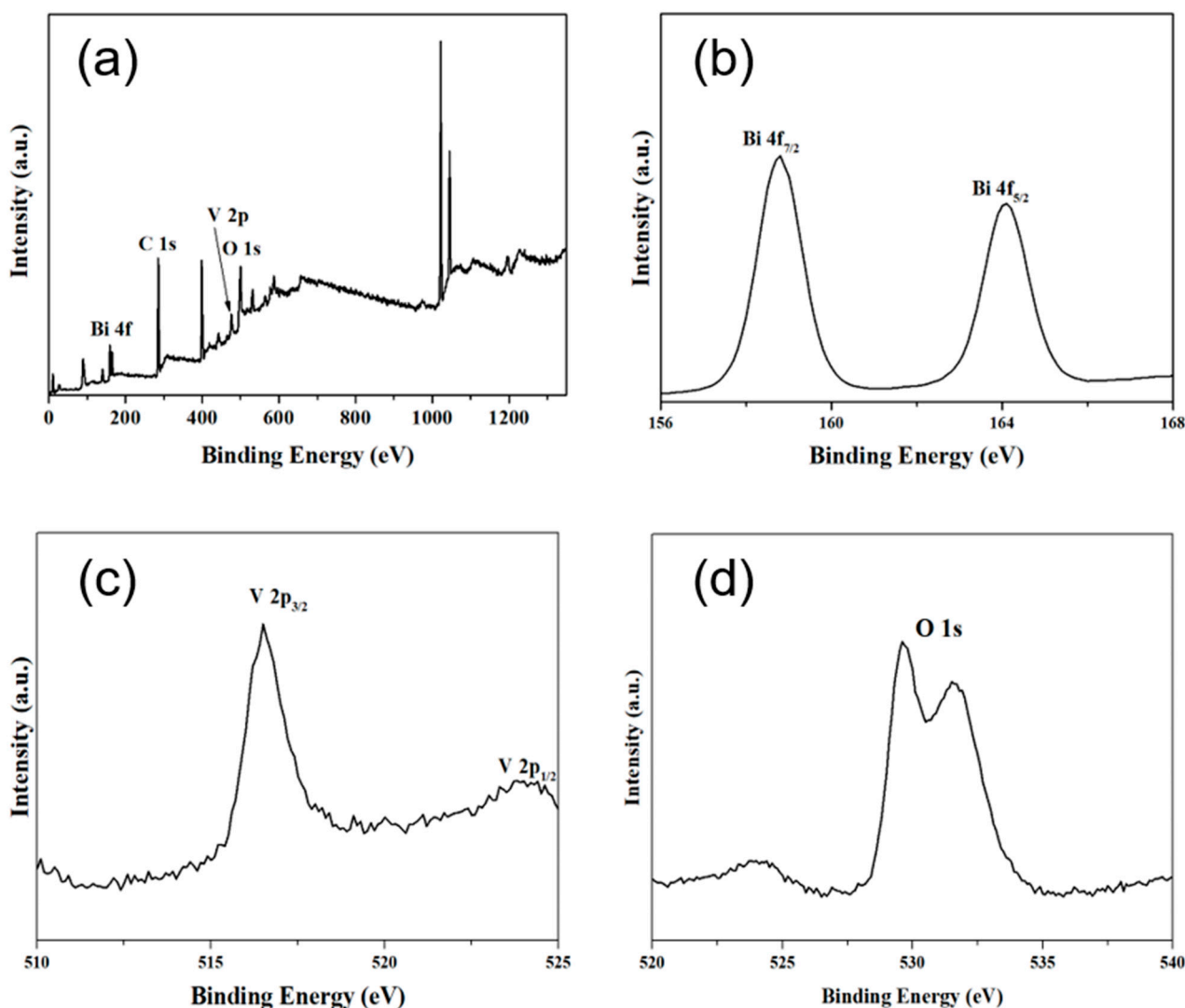


**Figure 3.** (a) XPS spectra of  $\text{BiVO}_4$  showing the presence of Bi, C, O and V. High-resolution XPS spectra showing: (b) Bi 4f at 158.5 and 164.4 eV, (c) V 2p 516.5 eV and 524.3 eV and (d) O 1s at 528.9 and 532.5 eV.

Specific surface areas of  $\text{BiVO}_4$  and  $\text{BiVO}_4@ \text{ZIF}-8$  were obtained using nitrogen adsorption–desorption tests. Owing to the addition of mesoporous ZIF–8, the as-prepared  $\text{BiVO}_4@ \text{ZIF}-8$  composite showed a type IV hysteresis loop, as seen in Figure 4b [20]. Moreover, as calculated via the instrument, the surface area of  $\text{BiVO}_4@ \text{ZIF}-8$  was as high as  $304.5 \text{ m}^2/\text{g}$ , which was much larger than that of pure  $\text{BiVO}_4$  ( $2.53 \text{ m}^2/\text{g}$ ). Owing to its larger surface area,  $\text{BiVO}_4@ \text{ZIF}-8$  had more active sites to absorb and degrade organic dyes than pure  $\text{BiVO}_4$ ; thus, the catalytic performance could be significantly enhanced.

The property of light absorption was another crucial factor that affected the photocatalytic properties of  $\text{BiVO}_4$  and  $\text{BiVO}_4@ \text{ZIF}-8$ . Therefore, ultraviolet–visible absorption spectra were applied to characterize the light absorption abilities of  $\text{BiVO}_4$  and  $\text{BiVO}_4@ \text{ZIF}-8$ . From the spectra in Figure 5, we can see that the absorption edges of pure  $\text{BiVO}_4$  and  $\text{BiVO}_4@ \text{ZIF}-8$  composites were all around 500 nm. Tauc’s equation, as shown in Equation (2), was applied to determine the band gap value of semiconductors with a direct band gap:

$$\alpha h\nu = A(h\nu - E_g)^{\frac{1}{2}} \quad (2)$$

where  $h$ ,  $\nu$ ,  $A$ ,  $E_g$  and  $\alpha$  represent Planck’s constant, light frequency, absorbance, band gap value and absorption coefficient, respectively. In Equation (2), the parameters  $A$  and  $\alpha$  are constant for a specific sample.

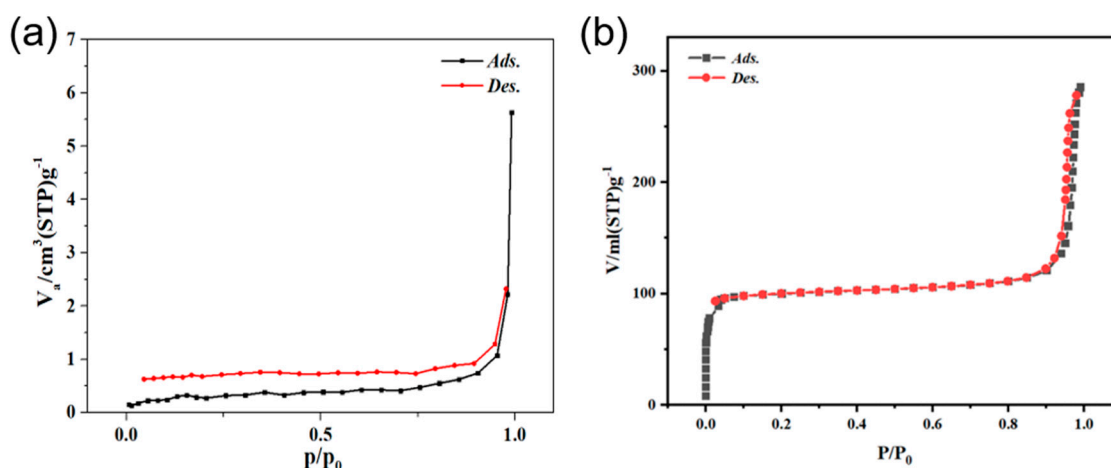


**Figure 4.** (a) The  $N_2$  adsorption–desorption isotherm of  $BiVO_4$  nanorods; (b) the  $N_2$  adsorption–desorption isotherm of  $BiVO_4@ZIF-8$ .

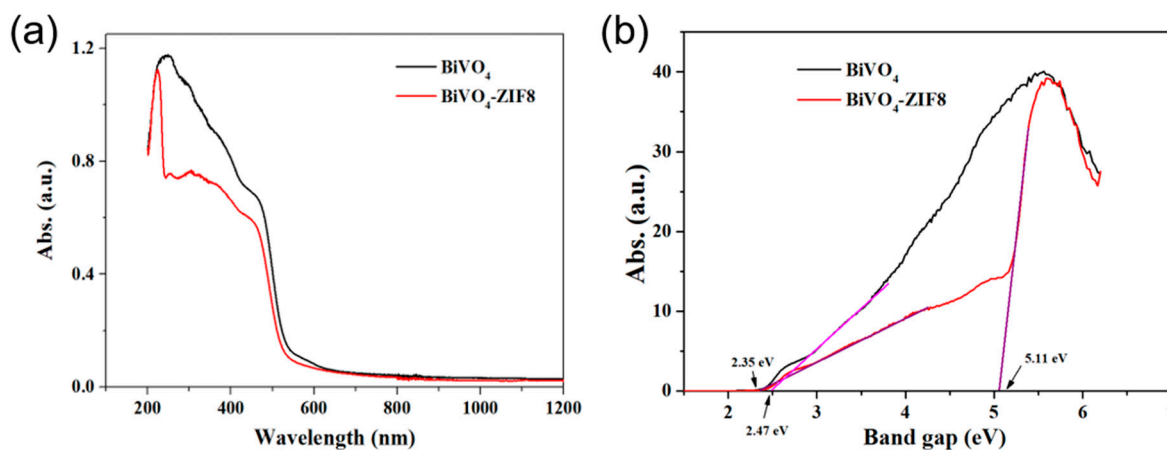


**Figure 5.** (a) The UV–Vis absorption curves of pure  $BiVO_4$  (black) and  $BiVO_4@ZIF-8$  (red); (b) the corresponding Kubelka–Munk (K–M) transformed curves of pure  $BiVO_4$  (black) and  $BiVO_4@ZIF-8$  (red). The band gaps for  $BiVO_4@ZIF-8$  and pure  $BiVO_4$  were calculated as 2.35 eV and 2.47 eV, respectively.

Figure 5b shows the K–M transformed reflectance spectra corresponding to Figure 5a. Extrapolating the quasi-straight line to intersect with the X-axis can provide the band gap values of the measured samples. As calculated in Figure 5b,  $BiVO_4$  without modification showed a band gap value of 2.47 eV. However, as shown in Figure 5b, after modification with ZIF–8, the band gap value for  $BiVO_4@ZIF-8$  was divided into two values: 2.35 eV and 5.11 eV. The latter was assigned to the value for ZIF–8. In addition, the band gap value for  $BiVO_4$  after modification with ZIF–8 (2.35 eV) was slightly narrower than that of pure  $BiVO_4$  in our research and other papers [31,32,38,39]. Smaller band gaps are typically more favorable for efficient utilization of solar energy to produce photogenerated electron–hole pairs, which could directly enhance the photocatalytic properties.

When the photogenerated electrons and holes are recombining, strong photoluminescence signals will occur and can be detected via PL spectra, as shown in Figure 6. The PL spectra of  $BiVO_4$  and  $BiVO_4@ZIF-8$  were both excited at 365 nm, which corresponded to a photon energy of 3.39 eV, and was larger than the band gap of both  $BiVO_4$  (2.47 eV) and  $BiVO_4@ZIF-8$  (2.35 eV). This energy was strong enough for both  $BiVO_4$  and  $BiVO_4@ZIF-8$  to excite valence electrons to the conduction band. As shown in Figure 6, the specific peak intensities of  $BiVO_4@ZIF-8$  at 540 nm were much weaker than those of pure  $BiVO_4$ . The weaker PL intensity indicated that the recombination of photogenerated electrons and

holes was largely suppressed in the  $\text{BiVO}_4@\text{ZIF}-8$  composite, which was conducive to enhancing photocatalytic performance [40].

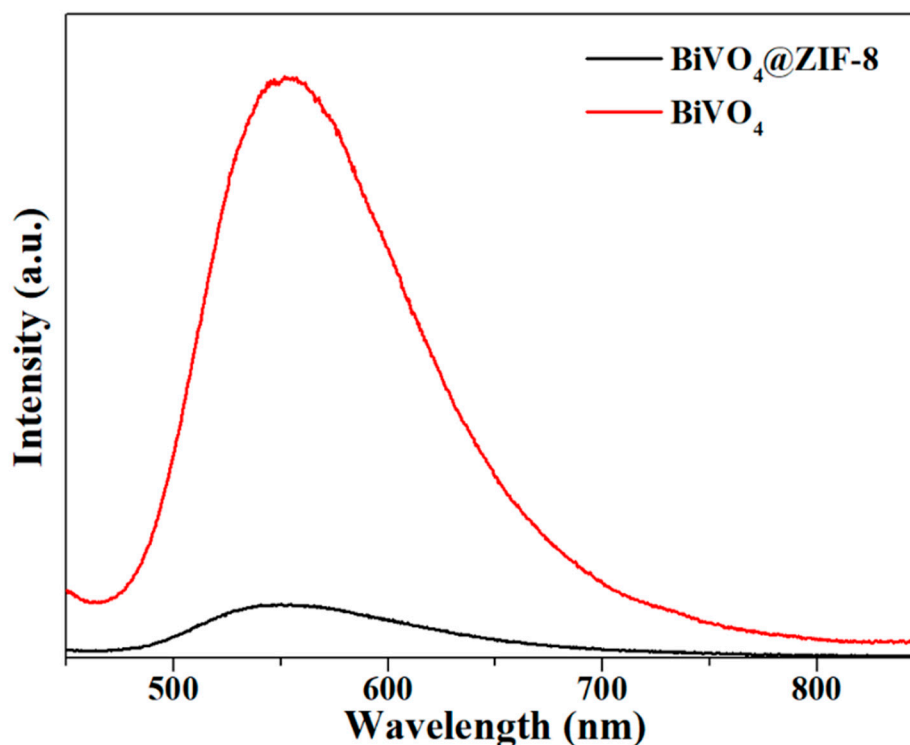


**Figure 6.** The PL spectrum of  $\text{BiVO}_4$  and  $\text{BiVO}_4@\text{ZIF}-8$ ; the PL intensity of  $\text{BiVO}_4@\text{ZIF}-8$  is much weaker than that for pure  $\text{BiVO}_4$ .

The photocatalytic performance of pure  $\text{BiVO}_4$  nanorods and  $\text{BiVO}_4@\text{ZIF}-8$  composites was evaluated by RhB photodegradation tests, as shown in Figure 7. Figure 7a shows the RhB degradation efficiencies of pure  $\text{BiVO}_4$  nanorods and  $\text{BiVO}_4@\text{ZIF}-8$  composites under UV light and visible light at different degradation times. As shown in Equation (1), the degradation efficiency of RhB was determined via UV-Vis absorption spectra, as presented in Figure S2. It is noticeable that about 15% to 23% of RhB was missing before the light irradiation of pure  $\text{BiVO}_4$  and  $\text{BiVO}_4@\text{ZIF}-8$ , respectively, mainly due to the adsorption characteristics of  $\text{BiVO}_4$  and  $\text{BiVO}_4@\text{ZIF}-8$ . Owing to the larger surface area, more RhB will be absorbed by  $\text{BiVO}_4@\text{ZIF}-8$  than by pure  $\text{BiVO}_4$ . When RhB is dissolved in water, it is positively charged. Therefore, RhB cations will be attracted by the  $\text{O}^{2-}$  or  $\text{OH}^-$  anions at the photocatalyst's surface. As shown in Figure 7a, after being irradiated under visible light for 40 min, about 80% of RhB was degraded by  $\text{BiVO}_4@\text{ZIF}-8$ , while 32% of RhB still remained with the pure  $\text{BiVO}_4$  nanorods. It can also be seen in Figure 7a that, under full-spectrum irradiation, more than 90% of RhB was degraded by  $\text{BiVO}_4@\text{ZIF}-8$  in 20 min and entirely decomposed after 60 min. In comparison, after being irradiated under UV light for 20 min, less than 70% of RhB was degraded by the pure  $\text{BiVO}_4$  nanorods, and still 20% of RhB remained after irradiation for 40 min. The photocatalytic property of pure ZIF-8 is also shown in Figure S2e,f, which show that over 60% of RhB was absorbed by the MOF, owing to its large surface area and mesoporous structure. However, only about 80% of RhB was degraded during the following photodegradation.

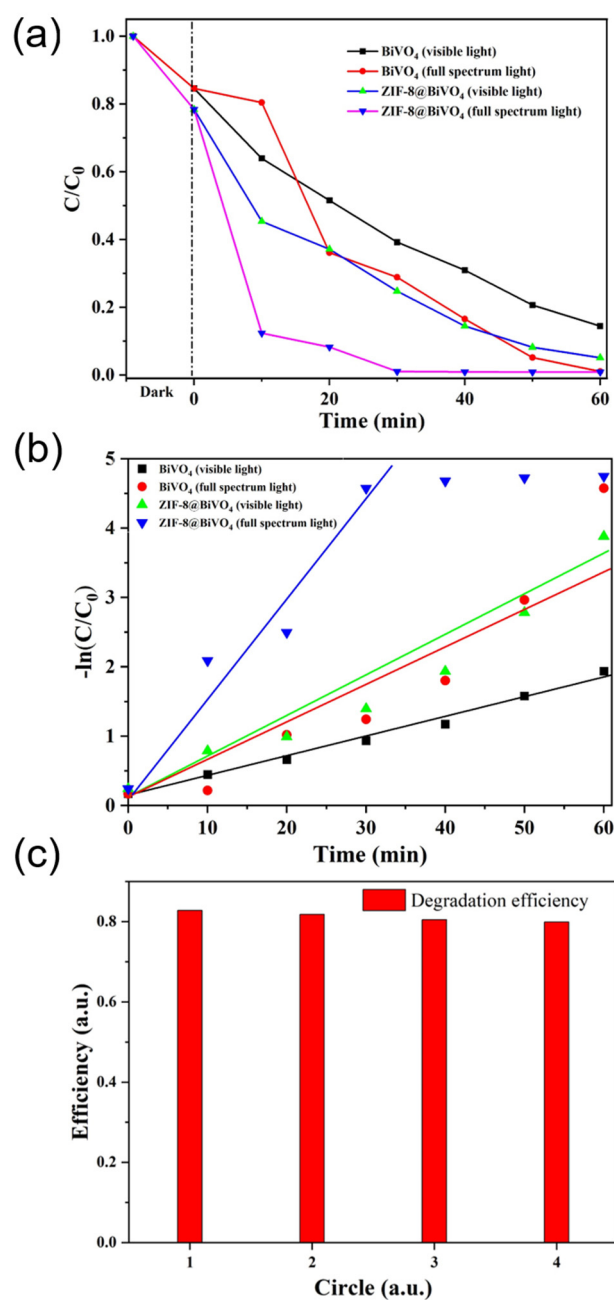


**Figure 7.** (a) The photodegradation efficiency of BiVO<sub>4</sub> and BiVO<sub>4</sub>@ZIF-8 under full-spectrum and visible light. In the presence of BiVO<sub>4</sub>-ZIF 8, more than 90% of RhB is degraded after 60 min of visible light irradiation, while only 80% of RhB is degraded in the presence of pure BiVO<sub>4</sub>. (b) The value of  $\ln(C_0/C)$  vs. time for RhB degradation; BiVO<sub>4</sub>@ZIF-8 shows a higher kinetic constant with the value of  $0.133 \text{ min}^{-1}$ . (c) The reproducibility test of photocatalysis.

At a relatively low concentration (10 mg/L) of RhB solution, the kinetics of the degradation process of RhB could be defined as the pseudo-first-order reaction mode, which means that the values of the logarithm of the concentration ratio ( $\ln(C_0/C)$ ) and irradiation time have a linear relationship [41]. Therefore, the kinetic constant of  $k$  for RhB degradation was defined as the slope of the quasi-line of the logarithm of the concentration ratio and irradiation time, as illustrated in Figure 7b. After calculation, the value of  $k$  for BiVO<sub>4</sub> was  $0.05 \text{ min}^{-1}$ . The  $k$  value for BiVO<sub>4</sub>@ZIF-8 reached  $0.133 \text{ min}^{-1}$ , which indicates that BiVO<sub>4</sub>@ZIF-8 showed better photocatalytic activity under solar irradiation than pure BiVO<sub>4</sub>. Being as important as the catalytic efficiency, excellent reproducibility is

also a crucial factor for photocatalysts. In Figure 7c, the reproducibility of BiVO<sub>4</sub>@ZIF-8 was examined by recycling BiVO<sub>4</sub>@ZIF-8 for four cycles. The results show that the degradation efficiency of BiVO<sub>4</sub>@ZIF-8 was stable with no drastic deactivation after recycling, indicating its feasibility for practical applications such as water purification.

Figure 8 shows the photocatalysis mechanism in the presence of pure BiVO<sub>4</sub> and BiVO<sub>4</sub>@ZIF-8. As a type of semiconductor, the valence band (VB) is full of electrons, while the conduction band (CB) lacks electrons. When a semiconductor is irradiated under light with energy no less than the E<sub>g</sub> of that semiconductor, the light can excite the electrons at the VB to the CB. Therefore, holes will be left in the VB, and thus photogenerated electron-hole pairs will be formed. The photogenerated electron-hole pairs can oxidize H<sub>2</sub>O molecules, OH<sup>-</sup> ions and dissolved O<sub>2</sub> in H<sub>2</sub>O to form ·OH or O<sub>2</sub><sup>-·</sup> radicals, which have strong oxidation properties. Moreover, the organic dye RhB, with its characteristic absorption wavelength of about 550 nm, could be photosensitized under light as well. Therefore, the sensitized RhB dye could be oxidized into water and CO<sub>2</sub> by ·OH or O<sub>2</sub><sup>-·</sup> radicals, which is one of the possible degradation mechanisms of an organic dye. We may summarize the set of RhB degradation processes as shown in Equations (3)–(6) below [42]:

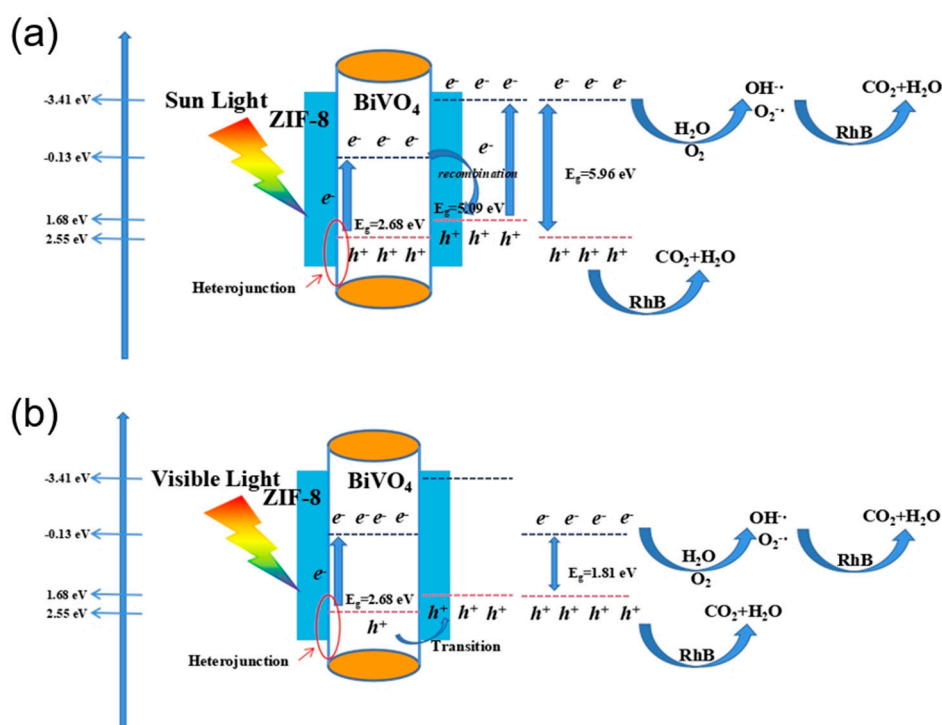
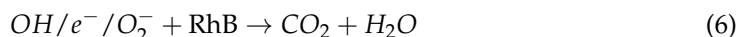


**Figure 8.** The working mechanism of RhB photodegradation under (a) sunlight and (b) visible light.

In Equation (6), there are two pathways involved in RhB degradation: the stepwise de-ethylation process, and cleavage of the conjugated hydrocarbon structure [43,44], which can be directly seen in the UV-Vis absorption curve in Figure S2. The cleavage of the conjugated hydrocarbon structure leads to a decreased absorption intensity of the RhB solution, and the de-ethylation process leads to the red shift in the absorption peak of RhB to about 500 nm.

The mechanism of the enhanced photocatalysis performance of BiVO<sub>4</sub>@ZIF-8 could be further explained by its band gap structure. The positions of the CB and VB for BiVO<sub>4</sub> and ZIF-8 are clearly shown in Figure 8. For the BiVO<sub>4</sub>@ZIF-8 heterojunction structure, the VB and CB positions of BiVO<sub>4</sub> are all much more positive than those of ZIF-8 (the CB and VB positions are -0.13 eV and 2.55 eV for BiVO<sub>4</sub>, respectively, and -3.41 eV and 1.68 eV for ZIF-8, respectively). Hence, we may discuss the enhancing mechanism under both UV light and visible light. When irradiated under UV light, the photogenerated electron-hole pairs can be generated from both BiVO<sub>4</sub> and ZIF-8 at the CB and VB, respectively. Owing to the closer position of the CB of BiVO<sub>4</sub> and the VB of ZIF-8, the electron at the conduction band of BiVO<sub>4</sub> and the hole at the valence band of ZIF-8 tend to recombine with each other more easily. Therefore, the e<sup>-</sup> and h<sup>+</sup> of BiVO<sub>4</sub>@ZIF-8 only remain at the CB of ZIF-8 and the VB of BiVO<sub>4</sub>, respectively, which indicates that the band gap width of BiVO<sub>4</sub>@ZIF-8 is extended to 5.96 eV. The O<sub>2</sub><sup>-·</sup> at the CB of ZIF-8 has higher energy than that of BiVO<sub>4</sub>; therefore, BiVO<sub>4</sub>@ZIF-8 is more beneficial for RhB degradation. When irradiated under visible light, due to the larger band gap of ZIF-8, the photogenerated electron-hole pairs can only be excited at the BiVO<sub>4</sub> surface. As the VB of ZIF-8 is more negative than that of BiVO<sub>4</sub>, the covalent Bi-O-Zn at the heterojunction could play a role that transfers the holes at the VB of BiVO<sub>4</sub> to the VB of ZIF-8 and hinders the recombination of the photogenerated electron-hole pairs [45]. In addition, the processes of degradation often occur at the surfaces of photocatalysts; in the BiVO<sub>4</sub>@ZIF-8 composite, ZIF-8, with its mesoporous structure and large surface area, has more active sites for h<sup>+</sup> to form free radicals to photodegrade RhB. Thus, BiVO<sub>4</sub>@ZIF-8, with its larger surface area and heterojunction structures, exhibited better photocatalysis performance.

As a class of multiple functional materials, BiVO<sub>4</sub> and its composites have been widely applied in the field of water treatment via photodegradation. Therefore, we investigated the degradation efficiency via photocatalysis of different photocatalysts based on BiVO<sub>4</sub> composite materials, as listed in Table S1. In addition, we investigated the performance of different photocatalysts based on ZIF-8 composite materials, as illustrated in Table S2. As shown in Table S2, the BiVO<sub>4</sub>@ZIF-8 heterojunction had a better catalysis performance than other BiVO<sub>4</sub>- or ZIF-8-based composite materials.

#### 4. Conclusions

In conclusion, BiVO<sub>4</sub>@ZIF-8, with its larger surface area and heterojunction structure, was fabricated using a hydrothermal technique first, and then a self-sedimentation technique. Owing to its mesoporous surface and heterojunction structure, the as-synthesized BiVO<sub>4</sub>@ZIF-8 exhibited a higher degradation efficiency than that of pure BiVO<sub>4</sub>. As shown in our research, about 90% of RhB was degraded under 60 min of visible light irradiation. The high degradation efficiency and reproducibility demonstrate that BiVO<sub>4</sub>@ZIF-8, as designed in our work, could be a prominent candidate for wastewater treatment.

**Supplementary Materials:** The following are available online at <https://www.mdpi.com/article/10.3390/ma14237424/s1>, Figure S1: The XRD pattern (a) and the standard PDF card (b) of pure BiVO<sub>4</sub>. Figure S2: The light absorption spectra of RhB solution after photo-degraded by BiVO<sub>4</sub> (a) and BiVO<sub>4</sub>@ZIF-8 (b) in visible light; BiVO<sub>4</sub> (c), BiVO<sub>4</sub>@ZIF-8 (d) and pure ZIF-8 (e) in UV light; (f) The photo degradation efficiency of pure ZIF-8 under UV light. Table S1: The performances of photocatalysts based on different BiVO<sub>4</sub> composite materials. Table S2: The performances of photocatalysts based on different MOF composite materials.

**Author Contributions:** Conceptualization, R.G. and H.Z.; data curation, R.G., Y.X., M.L. and T.B.; funding acquisition, C.P. and H.Z.; investigation, R.G., C.P. and H.Z.; methodology, R.G. and Y.X.; resources, H.Z.; supervision, C.P. and H.Z.; writing—original draft, R.G.; writing—review and editing, Y.X., M.L., T.B., C.P. and H.Z. All authors have read and agreed to the published version of the manuscript.

**Funding:** This research was funded by start-up funding from ShanghaiTech University (for H.Z. and C.P.), the National Natural Science Foundation of China (Grant No. 11902200 for H.Z. and 21902142 for C.P.) and the Shanghai Sailing Program (Grant 19YF1433600).

**Institutional Review Board Statement:** Not applicable.

**Informed Consent Statement:** Not applicable.

**Data Availability Statement:** The data supporting reported results of the current study are available from the corresponding authors on reasonable request.

**Acknowledgments:** The authors acknowledge support from the Centre for High-resolution Electron Microscopy (ChEM) (#EM02161943), and the Analytical Instrumentation Center (#SPST-AIC10112914), SPST, ShanghaiTech University.

**Conflicts of Interest:** The authors declare no conflict of interest.

## References

1. An, J.; Zhou, Q. Degradation of some typical pharmaceuticals and personal care products with copper-plating iron doped Cu<sub>2</sub>O under visible light irradiation. *J. Environ. Sci.* **2012**, *24*, 827–833. [[CrossRef](#)]
2. Kitsiou, V.; Filippidis, N.; Mantzavinos, D.; Poullos, I. Heterogeneous and homogeneous photocatalytic degradation of the insecticide imidacloprid in aqueous solutions. *Appl. Catal. B Environ.* **2009**, *86*, 27–35. [[CrossRef](#)]
3. Jiang, J.; Wang, H.; Chen, X.; Li, S.; Xie, T.; Wang, D.; Lin, Y. Enhanced photocatalytic degradation of phenol and photogenerated charges transfer property over BiOI-loaded ZnO composites. *J. Colloid Interface Sci.* **2017**, *494*, 130–138. [[CrossRef](#)]
4. Tian, L.; Rui, Y.; Sun, K.; Cui, W.; An, W. Surface Decoration of ZnWO<sub>4</sub> Nanorods with Cu<sub>2</sub>O Nanoparticles to Build Heterostructure with Enhanced Photocatalysis. *Nanomaterials* **2018**, *8*, 33. [[CrossRef](#)]
5. Kisch, H. Semiconductor Photocatalysis—Mechanistic and Synthetic Aspects. *Angew. Chem. Int. Ed.* **2013**, *52*, 812–847. [[CrossRef](#)] [[PubMed](#)]
6. Xu, Y.-S.; Zhang, W.-D. Monodispersed Ag<sub>3</sub>PO<sub>4</sub> nanocrystals loaded on the surface of spherical Bi<sub>2</sub>MoO<sub>6</sub> with enhanced photocatalytic performance. *Dalton Trans.* **2013**, *42*, 1094–1101. [[CrossRef](#)] [[PubMed](#)]
7. Andersson, M.; Österlund, L.; Ljungström, S.; Palmqvist, A. Preparation of Nanosize Anatase and Rutile TiO<sub>2</sub> by Hydrothermal Treatment of Microemulsions and Their Activity for Photocatalytic Wet Oxidation of Phenol. *J. Phys. Chem. B* **2022**, *106*, 10674–10679. [[CrossRef](#)]
8. Deng, D.; Martin, S.T.; Ramanathan, S. Synthesis and characterization of one-dimensional flat ZnO nanotower arrays as high-efficiency adsorbents for the photocatalytic remediation of water pollutants. *Nanoscale* **2010**, *2*, 2685–2691. [[CrossRef](#)] [[PubMed](#)]
9. Wang, H.; Sun, F.; Zhang, Y.; Gu, K.; Chen, W.; Li, W. Photochemical construction of free-standing Sn-filled SnO<sub>2</sub> nanotube array on a solution surface for flexible use in photocatalysis. *J. Mater. Chem.* **2011**, *21*, 12407–12413. [[CrossRef](#)]
10. Zhao, X.; Liu, H.; Qu, J. Photoelectrocatalytic degradation of organic contaminants at Bi<sub>2</sub>O<sub>3</sub>/TiO<sub>2</sub> nanotube array electrode. *Appl. Surf. Sci.* **2011**, *257*, 4621–4624. [[CrossRef](#)]
11. Mohan, S.; Subramanian, B. A strategy to fabricate bismuth ferrite (BiFeO<sub>3</sub>) nanotubes from electrospun nanofibers and their solar light-driven photocatalytic properties. *RSC Adv.* **2013**, *3*, 23737–23744. [[CrossRef](#)]
12. Monfort, O.; Sfaelou, S.; Satrapinsky, L.; Plecenik, T.; Roch, T.; Plesch, G.; Lianos, P. Comparative study between pristine and Nb-modified BiVO<sub>4</sub> films employed for photoelectrocatalytic production of H<sub>2</sub> by water splitting and for photocatalytic degradation of organic pollutants under simulated solar light. *Catal. Today* **2017**, *280*, 51–57. [[CrossRef](#)]
13. Zhao, Q.; Ju, D.; Song, X.; Deng, X.; Ding, M.; Xu, X.; Zeng, H. Polyhedral Zn<sub>2</sub>SnO<sub>4</sub>: Synthesis, enhanced gas sensing and photocatalytic performance. *Sens. Actuators B Chem.* **2016**, *229*, 627–634. [[CrossRef](#)]
14. Di, L.J.; Yang, H.; Hu, G.; Xian, T.; Ma, J.Y.; Jiang, J.L.; Li, R.S.; Wei, Z.Q. Enhanced photocatalytic activity of BiFeO<sub>3</sub> particles by surface decoration with Ag nanoparticles. *J. Mater. Sci. Mater. Electron.* **2014**, *25*, 2463–2469. [[CrossRef](#)]
15. Obregón, S.; Colón, G. Heterostructured Er<sup>3+</sup> doped BiVO<sub>4</sub> with exceptional photocatalytic performance by cooperative electronic and luminescence sensitization mechanism. *Appl. Catal. B Environ.* **2014**, *158–159*, 242–249. [[CrossRef](#)]
16. Dolić, S.D.; Jovanović, D.J.; Smits, K.; Babić, B.; Marinović-Cincović, M.; Porobić, S.; Dramićanin, M.D. A comparative study of photocatalytically active nanocrystalline tetragonal zircon-type and monoclinic scheelite-type bismuth vanadate. *Ceram. Int.* **2018**, *44*, 17953–17961. [[CrossRef](#)]
17. Liang, Z.; Cao, Y.; Qin, H.; Jia, D. Low-heating solid-state chemical synthesis of monoclinic scheelite BiVO<sub>4</sub> with different morphologies and their enhanced photocatalytic property under visible light. *Mater. Res. Bull.* **2016**, *84*, 397–402. [[CrossRef](#)]
18. Tokunaga, S.; Kato, H.; Kudo, A. ChemInform Abstract: Selective Preparation of Monoclinic and Tetragonal BiVO<sub>4</sub> with Scheelite Structure and Their Photocatalytic Properties. *ChemInform* **2002**, *33*, 4624–4628. [[CrossRef](#)]
19. Guo, L.; Li, J.; Lei, N.; Song, Q.; Liang, Z. Morphological evolution and enhanced photoelectrochemical performance of V<sup>4+</sup> self-doped, [010] oriented BiVO<sub>4</sub> for water splitting. *J. Alloy. Compd.* **2019**, *771*, 914–923. [[CrossRef](#)]
20. Ge, L.; Liu, J. Efficient visible light-induced photocatalytic degradation of methyl orange by QDs sensitized CdS-Bi<sub>2</sub>WO<sub>6</sub>. *Appl. Catal. B Environ.* **2011**, *105*, 289–297. [[CrossRef](#)]

21. Hong, S.J.; Lee, S.; Jang, J.S.; Lee, J.S. Heterojunction BiVO<sub>4</sub>/WO<sub>3</sub> electrodes for enhanced photoactivity of water oxidation. *Energy Environ. Sci.* **2011**, *4*, 1781–1787. [[CrossRef](#)]
22. Xi, G.; Ye, J. Synthesis of bismuth vanadate nanoplates with exposed {001} facets and enhanced visible-light photocatalytic properties. *Chem. Commun.* **2010**, *46*, 1893–1895. [[CrossRef](#)]
23. Xia, Y.; Shang, S.-k.; Zeng, X.-r.; Zhou, J.; Li, Y.-y. A Novel Bi<sub>2</sub>MoO<sub>6</sub>/ZIF–8 Composite for Enhanced Visible Light Photocatalytic Activity. *Nanomaterials* **2019**, *9*, 545. [[CrossRef](#)] [[PubMed](#)]
24. Li, H.; Jiang, L.; Dong, W.; Zhang, E.; Ji, Z. Preparation and characterization of ZnO/ZIF–8 composite with selective photoelectrochemical responses. *Mater. Lett.* **2017**, *201*, 165–168. [[CrossRef](#)]
25. Zhang, B.; Zhang, J.; Tan, X.; Shao, D.; Shi, J.; Zheng, L.; Zhang, J.; Yang, G.; Han, B. MIL-125-NH<sub>2</sub>@TiO<sub>2</sub> Core–Shell Particles Produced by a Post-Solvothermal Route for High-Performance Photocatalytic H<sub>2</sub> Production. *ACS Appl. Mater. Interfaces* **2018**, *10*, 16418–16423. [[CrossRef](#)]
26. Li, X.; Pi, Y.; Hou, Q.; Yu, H.; Li, Z.; Li, Y.; Xiao, J. Amorphous TiO<sub>2</sub>@NH<sub>2</sub>-MIL-125(Ti) homologous MOF-encapsulated heterostructures with enhanced photocatalytic activity. *Chem. Commun.* **2018**, *54*, 1917–1920. [[CrossRef](#)]
27. Xu, J.; Gao, J.; Wang, C.; Yang, Y.; Wang, L. NH<sub>2</sub>-MIL-125(Ti)/graphitic carbon nitride heterostructure decorated with NiPd co-catalysts for efficient photocatalytic hydrogen production. *Appl. Catal. B Environ.* **2017**, *219*, 101–108. [[CrossRef](#)]
28. Liang, P.; Zhang, C.; Sun, H.; Liu, S.; Tade, M.; Wang, S. Photocatalysis of C, N-doped ZnO derived from ZIF–8 for dye degradation and water oxidation. *RSC Adv.* **2016**, *6*, 95903–95909. [[CrossRef](#)]
29. Wang, D.; Li, Z.; Zhou, J.; Fang, H.; He, X.; Jena, P.; Zeng, J.-B.; Wang, W.-N. Simultaneous Detection and Removal of Formaldehyde at Room Temperature: Janus Au@ZnO@ZIF–8 Nanoparticles. *Nano-Micro Lett.* **2017**, *10*, 4. [[CrossRef](#)]
30. Shao, C.; Feng, S.; Zhu, G.; Zheng, W.; Sun, J.; Huang, X.; Ni, Z. Synergistic effects in N-K<sub>2</sub>Ti<sub>4</sub>O<sub>9</sub>/ZIF–8 composite and its photocatalysis degradation of Bisphenol A. *Mater. Lett.* **2020**, *268*, 127334. [[CrossRef](#)]
31. Lin, Y.; Lu, C.; Wei, C. Microstructure and photocatalytic performance of BiVO<sub>4</sub> prepared by hydrothermal method. *J. Alloy. Compd.* **2019**, *781*, 56–63. [[CrossRef](#)]
32. Zhang, Y.; Guo, Y.; Duan, H.; Li, H.; Sun, C.; Liu, H. Facile synthesis of V<sup>4+</sup> self-doped, [010] oriented BiVO<sub>4</sub> nanorods with highly efficient visible light-induced photocatalytic activity. *Phys. Chem. Chem. Phys.* **2014**, *16*, 24519–24526. [[CrossRef](#)]
33. Joo, J.B.; Zhang, Q.; Dahl, M.; Zaera, F.; Yin, Y. Synthesis, crystallinity control, and photocatalysis of nanostructured titanium dioxide shells. *J. Mater. Res.* **2013**, *28*, 362–368. [[CrossRef](#)]
34. Wu, J.; Lü, X.; Zhang, L.; Xia, Y.; Huang, F.; Xu, F. Crystallinity control on photocatalysis and photoluminescence of TiO<sub>2</sub>-based nanoparticles. *J. Alloy. Compd.* **2010**, *496*, 234–240. [[CrossRef](#)]
35. Wong, M.-S.; Hsu, S.-W.; Rao, K.K.; Kumar, C.P. Influence of crystallinity and carbon content on visible light photocatalysis of carbon doped titania thin films. *J. Mol. Catal. A Chem.* **2008**, *279*, 20–26. [[CrossRef](#)]
36. Yin, C.; Zhu, S.; Chen, Z.; Zhang, W.; Gu, J.; Zhang, D. One step fabrication of C-doped BiVO<sub>4</sub> with hierarchical structures for a high-performance photocatalyst under visible light irradiation. *J. Mater. Chem. A* **2013**, *1*, 8367–8378. [[CrossRef](#)]
37. Liu, Y.; Dai, H.; Deng, J.; Zhang, L.; Au, C.T. Three-dimensional ordered macroporous bismuth vanadates: PMMA-templating fabrication and excellent visible light-driven photocatalytic performance for phenol degradation. *Nanoscale* **2012**, *4*, 2317–2325. [[CrossRef](#)]
38. Kong, D.; Qi, J.; Liu, D.; Zhang, X.; Pan, L.; Zou, J. Ni-Doped BiVO<sub>4</sub> with V<sup>4+</sup> Species and Oxygen Vacancies for Efficient Photoelectrochemical Water Splitting. *Trans. Tianjin Univ.* **2019**, *25*, 340–347. [[CrossRef](#)]
39. Obregón, S.; Caballero, A.; Colón, G. Hydrothermal synthesis of BiVO<sub>4</sub>: Structural and morphological influence on the photocatalytic activity. *Appl. Catal. B Environ.* **2012**, *117–118*, 59–66. [[CrossRef](#)]
40. Zhang, T.; Liu, Y.; Jiang, S.; Li, B.; Wang, J.; Shao, X.; Wang, D.; Wang, K.; Yan, Z. Bacitracin-assisted synthesis of spherical BiVO<sub>4</sub> nanoparticles with C doping for remarkable photocatalytic performance under visible light. *CrystEngComm* **2020**, *22*, 1812–1821. [[CrossRef](#)]
41. Ma, D.; Shi, J.-W.; Zou, Y.; Fan, Z.; Ji, X.; Niu, C. Highly Efficient Photocatalyst Based on a CdS Quantum Dots/ZnO Nanosheets 0D/2D Heterojunction for Hydrogen Evolution from Water Splitting. *ACS Appl. Mater. Interfaces* **2017**, *9*, 25377–25386. [[CrossRef](#)]
42. Guo, R.; Tian, R.; Shi, D.; Li, H.; Liu, H. S-Doped ZnSnO<sub>3</sub> Nanoparticles with Narrow Band Gaps for Photocatalytic Wastewater Treatment. *ACS Appl. Nano Mater.* **2019**, *2*, 7755–7765. [[CrossRef](#)]
43. Wang, Q.; Chen, C.; Zhao, D.; Ma, W.; Zhao, J. Change of Adsorption Modes of Dyes on Fluorinated TiO<sub>2</sub> and Its Effect on Photocatalytic Degradation of Dyes under Visible Irradiation. *Langmuir* **2008**, *24*, 7338–7345. [[CrossRef](#)] [[PubMed](#)]
44. Lei, P.; Chen, C.; Yang, J.; Ma, W.; Zhao, J.; Zang, L. Degradation of Dye Pollutants by Immobilized Polyoxometalate with H<sub>2</sub>O<sub>2</sub> under Visible-Light Irradiation. *Environ. Sci. Technol.* **2005**, *39*, 8466–8474. [[CrossRef](#)] [[PubMed](#)]
45. Ding, Y.-H.; Zhang, X.-L.; Zhang, N.; Zhang, J.-Y.; Zhang, R.; Liu, Y.-F.; Fang, Y.-Z. A visible-light driven Bi<sub>2</sub>S<sub>3</sub>@ZIF–8 core–shell heterostructure and synergistic photocatalysis mechanism. *Dalton Trans.* **2018**, *47*, 684–692. [[CrossRef](#)] [[PubMed](#)]